ACS APPLIED MATERIALS & INTERFACES

www.acsami.org

Research Article

Inductor-Free Output Multiplier for Power Promotion and Management of Triboelectric Nanogenerators toward Self-Powered Systems

Xin Xia, Haoyu Wang, Philippe Basset, Yuyan Zhu, and Yunlong Zi*

Cite This: *ACS Appl. Mater. Interfaces* 2020, 12, 5892−5900

Read Online

ACCESS | Metrics & More | Article Recommendations | Supporting Information

ABSTRACT: The output voltage of triboelectric nanogenerators (TENGs) is much higher than the overload capacity of most commercial electronics, making it hard to power them directly; so the power-management solution is indispensable. In the meanwhile, it is critical for practical applications to enhance the output performance of the TENG toward its breakdown limit, which is usually ignored before. Here, an inductor-free output multiplier (OM) for power promotion and management of TENGs is proposed, with the breakdown effect considered. This OM, as expanded based on bennet's doubler, is theoretically studied and experimentally demonstrated to significantly enhance the output performance of the TENG within only a few working cycles. The charge output was enhanced by 7.6 times experimentally with the OM. An external capacitor and a switch are applied to realize a high energy extraction ratio of up to 196%, with the average charge output per cycle of ∼3−3.75 μC achieved. This OM circuit with the smart switch is suitable for power promotion of TENGs with variable capacitance and for power management of all TENGs. The OM circuit is demonstrated to ensure the high output performance of TENGs even at a low triboelectric charge density, which is crucial for broad applications of the TENG toward self-powered systems, potentially to be a solution for improving the output performance of TENGs working in harsh environments.

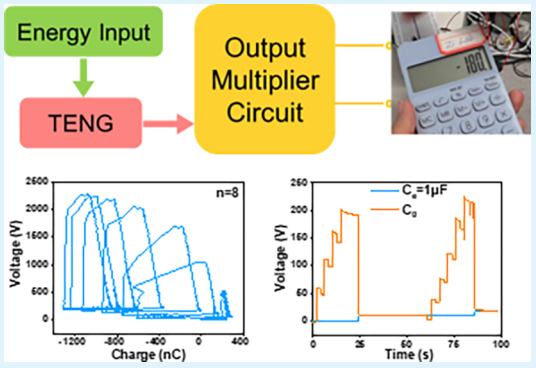

KEYWORDS: *triboelectric nanogenerator, breakdown effect, output enhancement, output multiplier, power management*

INTRODUCTION

To power widely distributed wireless sensor networks as well as portable and wearable electronics, triboelectric nanogenerators (TENGs)[1−7] have been invented to convert tiny energy from the environment into electricity, such as ocean wave,[8−11] wind,[12−15] human motions,[16−20] and vibration,[21−23] since 2012. Based on contact electrification coupling with the electrostatic induction,[24−26] the TENGs have a significant high-voltage output, which can be thousands of volts, but the charge output of the TENGs is very low, usually within 30 μC m^{-2}.[27] The bennet's doubler as proposed in the former research[28−30] has been demonstrated to greatly enhance the charge output of the TENGs,[31] and a series-parallel conditioning circuit has been developed based on the bennet's doubler theoretically, which can be used for the electrostatic energy harvesting as a charge pump, but there is no experimental demonstration.[32] However, these previous studies ignored the breakdown effect, which universally exists in TENGs and suppresses the charge output due to the electrostatic discharging;[33−36] therefore the optimized output performance of the TENG is still subject to further studies.

Meanwhile, because of the high-voltage but low-charge output of TENGs which induces the huge output impedance, it is extremely difficult for TENGs to directly power most commercial electronics with usually low impedance; thus power-management (PM) solutions are crucial for improving the compatibility of TENGs for powering electronics. Most of the existing PM solutions usually utilize inductors or transformers which can be considered as coupled inductors.[37−40] In these PM solutions, threshold working frequency, bandwidth, and power input are usually required, which cannot be easily satisfied by the low-frequency randomly pulsed power output of TENGs. At the same time, the bulky and high-weight inductors hindered the efforts to minimize TENG-based self-powered systems toward wearable and implantable applications. To develop inductor-free PM solutions, we have first proposed an effective energy storage strategy for TENGs, through automatic switches to maximize the energy storage efficiency up to 50%.[41] This idea is further developed to be a novel PM design based on automatic switches between serial-connected and parallel-connected capacitors, with 5-time charging rate demonstrated.[42] Even though these PM circuits

Received: November 5, 2019
Accepted: January 8, 2020
Published: January 8, 2020

https://dx.doi.org/10.1021/acsami.9b20060
ACS Appl. Mater. Interfaces 2020, 12, 5892−5900

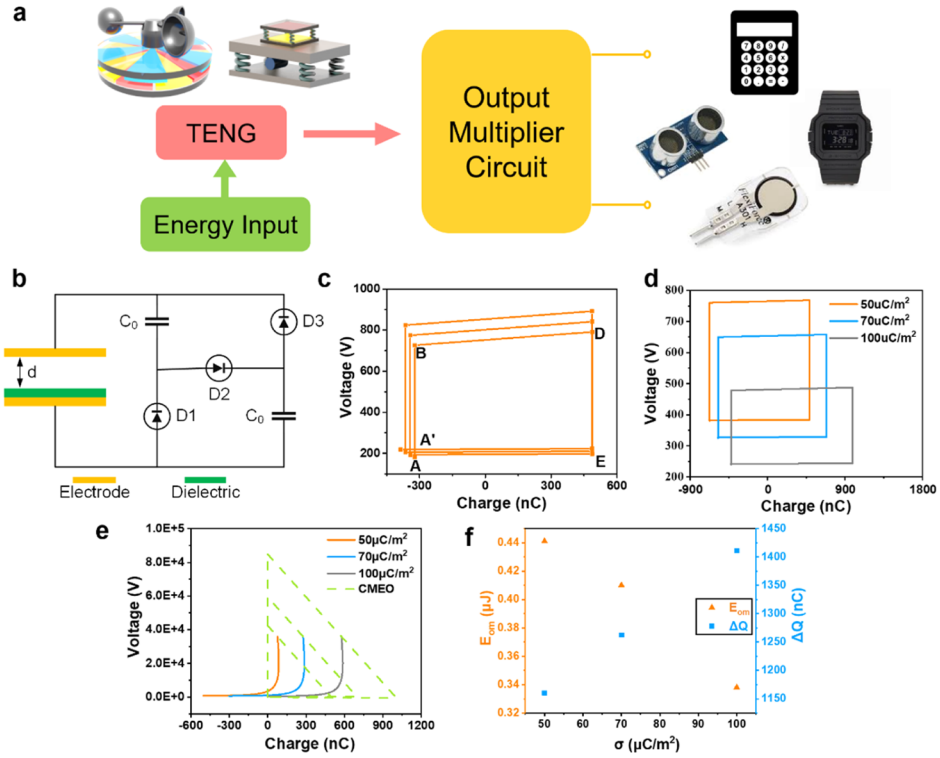

Figure 1. Properties of the CS mode TENG with bennet's doubler. (a) Introduction to the TENG system with the OM circuit. (b) Circuit of the CS mode TENG connected with the doubler. (c) Operation cycles of TENG under the doubler in $V-Q$ plot, with key points marked with letters. (d) Maximum cycles of TENG at different σ when breakdown happens. (e) Breakdown limits at different σ, with corresponding CMEO curve plotted in dash line. (f) Maximized energy output per cycle under OM, E_{om}, plotted in orange dots and ΔQ of the threshold cycle in blue vs σ.

have adjusted the output impedance of TENGs and enhanced overall efficiency, however, the circuit that can both enhance and manage the output performance of TENGs is still favored toward applications of TENGs as renewable power sources.

Here, we proposed a smart-designed circuit, in which the bennet's doubler is expanded to be an inductor-free output multiplier (OM), realizing the performance promotion and the PM for TENGs in the meanwhile within only a few working cycles. Starting from the working mechanism of the bennet's doubler, we first calculated operation cycles in the $V-Q$ plot of TENGs while connecting with the doubler. The maximized transferred charges ΔQ between the circuit and TENGs and the maximized energy output per cycle under OM E_{om} within the breakdown limits were studied, considering different surface charge density σ. To improve the performance, we developed an OM by expanding the doubler. Then, ΔQ, E_{om}, energy extraction ratio η, and cycles N required for TENGs to reach breakdown were theoretically simulated and experimentally demonstrated. We also proposed a charge enhancement ratio β to evaluate the performance of the OM and studied the effect of the capacitor number n. A motion-triggered switch with an external capacitor was applied to store energy from the OM, and the performance was evaluated. We also designed and built a smart switch to control the energy storage by avoiding breakdown automatically. This inductor-free OM circuit shows the great potential in charge promotion and PM even for the TENGs with the very low surface charge density, which will contribute a lot to the development of self-powered systems and applications in harsh environments.

THEORETICAL CALCULATIONS

Based on the working mechanism, the output performance of the TENG is determined by the surface charge density σ on the triboelectric layers,[6] which has been demonstrated to be limited by the breakdown effect.[16,43] The proposed circuit should be able to enhance the overall charge transfer while managing the output power. Figure 1a introduces the energy harvesting system when the TENG is connected with the OM circuit. The mechanical energy input is converted as the alternative electrostatic energy by the TENG, and after power promotion and management by the OM circuit, the effective energy output can be used to power portable electronics like calculators, watches, sensors, and so forth. Figure 1b illustrates the simplest circuit proposed based on the bennet's doubler as previously demonstrated,[31] including two capacitors C_0 and three diodes. This bennet's doubler circuit can be considered as the simplest version of the OM circuit with the capacitor number $n = 2$. The CS mode TENG is focused in this study, which has been demonstrated as a voltage source V connected in series with a variable capacitor.[7] The variable capacitance in the CS mode TENG can be calculated by the nonideal parallel-plate capacitance equation,[44] and the breakdown model has been well-developed.[27] Under operations with this bennet's doubler, the transferred charge and the output voltage of the CS mode TENG are increased cycle by cycle, until approaching the breakdown limit, as shown in Figure 1c, with several key points of the cycle marked. Parameters for theoretical calculations are listed in Table 1. The working mechanism of the proposed circuit is described in detail below. Starting at point A, when $d = 0$, the total capacitance C of the TENG reaches the maximized value C_m. We can assume the

https://dx.doi.org/10.1021/acsami.9b20060
ACS Appl. Mater. Interfaces 2020, 12, 5892−5900

Table 1. Parameters for Theoretical Calculations

length of the CS mode TENG, l	0.1 m
width of the CS mode TENG, w	0.1 m
triboelectric area, S	0.01 m^2
thickness of dielectric, d_r	FEP, 0.1 mm
dielectric constant, ε_r	2
capacitance between dielectric, C_2	1.77 nF
maximized separated displacement, d_{max}	0.01 m
capacitance of the circuit, C_0	300 nF
minimized capacitance between air gap of TENG, C_{1min} ($d = d_{max}$)	11.79 pF
initial voltage of C_0, V_i	0 V

initial voltage V on C_0 is V_i. From A to B, when d starts to increase (separation process), V will increase while C will decrease simultaneously. All diodes are off until $V < 2V_i$. For point B when $V = 2V_i$, D2 turns on while D1 and D3 are off, the two C_0 are connected in series, and TENG starts to charge the two capacitors until point D with the total transferred charge ΔQ. At point D, d reaches the maximized value d_{max} and the voltage also reaches the maximum of this cycle. From points D to E, tribo-layers of the CS mode TENG start to approach each other (contact process). V starts to decease, and all diodes turn off again. At point E, V decreases to the voltage V_D of C_0, which should be larger than V_i after charging. D2 turns off, and D1 and D3 turn on, so the two C_0 are connected in parallel. After that, d keeps decreasing, and the two C_0 will charge the TENG, each with the transferred charge of $\frac{1}{2}\Delta Q$. When the tribo-layers contact each other, the end-up voltage V_i' of the TENG will be larger than V_i. Then, the new working cycle will repeat the whole process as described above with the new initial voltage of V_i'. It should be noticed that after one working cycle, each C_0 obtains the charge of $\frac{1}{2}\Delta Q$. The transferred charge ΔQ is calculated by the following equation

$$\Delta Q = Q_D - Q_A = \frac{\frac{\sigma S}{C_{1min}} + V_i\left(\frac{C_2}{C_{1min}} - 1\right)}{\frac{2}{C_0} + \frac{1}{C_{1min}} + \frac{1}{C_2}} \quad (1)$$

$$V_i' = \frac{\frac{\sigma S}{C_{1min}} + 2V_i(C_0 + C_2)\left(\frac{1}{C_0} + \frac{1}{C_{1min}} + \frac{1}{C_2}\right)}{\left(\frac{2}{C_0} + \frac{1}{C_{1min}} + \frac{1}{C_2}\right)(2C_0 + C_2)} \quad (2)$$

The enhanced voltage V_i' is

Complete operation configurations and derivations are shown in Figure S1 and Note S1, respectively. The working principle of the circuit is based on the variable capacitance of the CS mode TENG, so it is also suitable for other TENGs with variable capacitance, such as the lateral-sliding mode TENG, for the power-promotion purpose.

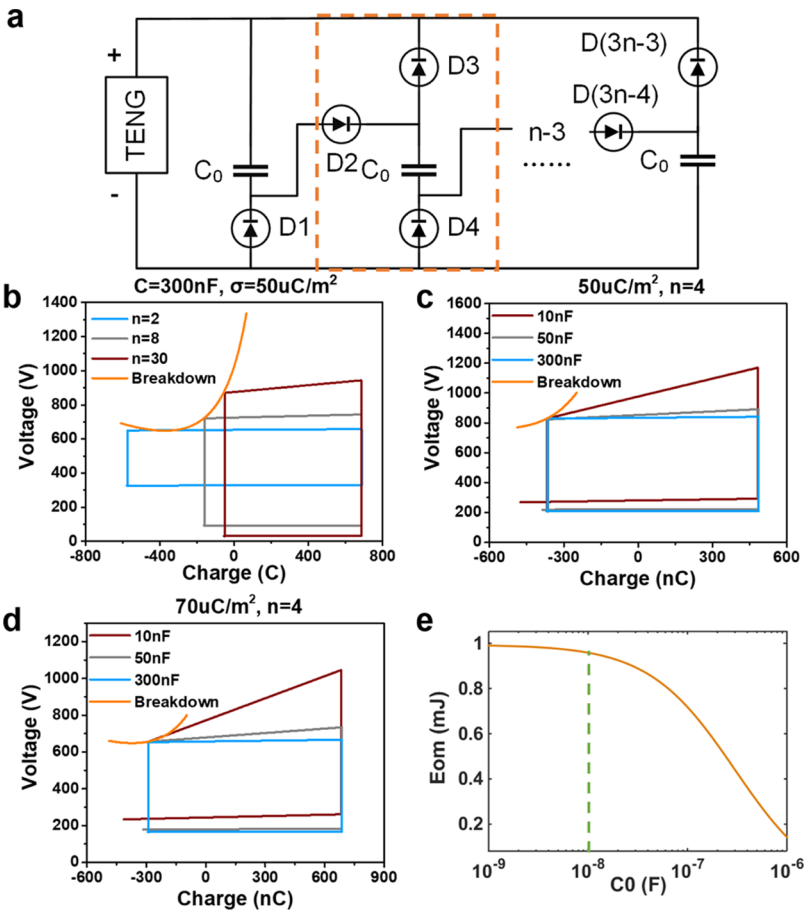

Figure 2. Properties of the CS mode TENG with the OM. (a) Circuit of the OM, with repeat components marked by an orange scheme. (b) Threshold cycles of different n in V–Q plot with C_0 = 300 nF, σ = 50 μC m^{-2}, compared with the breakdown curve. Key points are marked with letters. (c,d) Threshold cycles of different C_0 in V–Q plot at n = 4, σ = 50 μC m^{-2} and n = 4, σ = 70 μC m^{-2}, respectively, compared with the breakdown curve. (e) Relationship between E_{om} and C_0, with C_0 = 10 nF marked by a dash line in green.

https://dx.doi.org/10.1021/acsami.9b20060
ACS Appl. Mater. Interfaces 2020, 12, 5892–5900

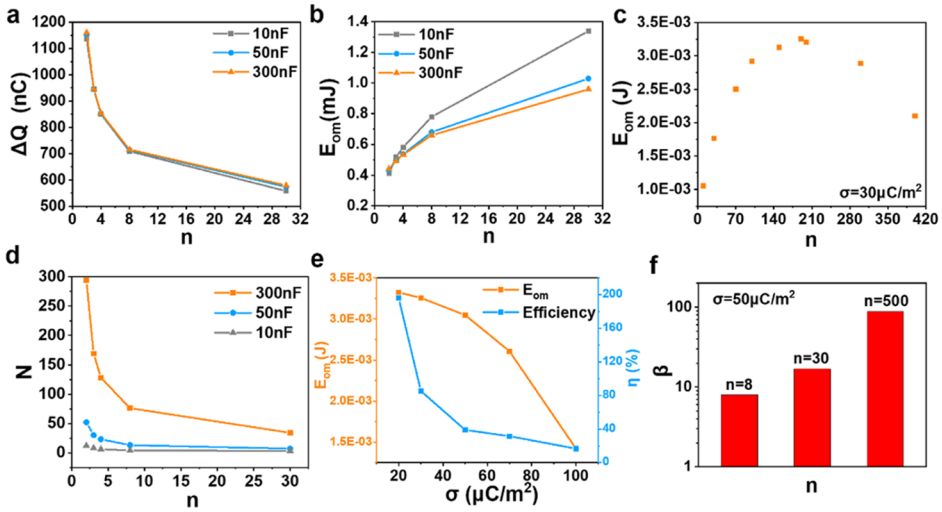

Figure 3. Performance of the OM with different parameters. (a) Comparison for ΔQ of the threshold cycle at different C_0 vs n. (b) Comparison for E_{om} at different C_0 vs n. (c) Relationship between E_{om} and n at σ = 30 μC m^{-2}, with maximized E_{om} shown at n = 190. (d) Comparison for N at different C_0 vs n. (e) Relationship between E_{om} and σ, compared with the corresponding η. (f) Summary of the charge enhancement ratio with different n at σ = 50 μC m^{-2}.

This implies that the output voltage of the TENG will be improved continuously while the TENG keeps working with the bennet's doubler circuit, indicating that the output charge will be enhanced after each working cycle. When the voltage between tribo-layers reaches the breakdown voltage as calculated by Paschen's law, air breakdown will happen and then the output will decrease to a lower level due to the breakdown discharge. Figure 1d shows the maximum cycle as limited by the breakdown effect of CS mode TENGs at different surface charge density. This indicates that air breakdown is more prone for the TENG at a larger σ while ΔQ is larger. Figure 1e shows the breakdown curve at different surface charge density, as compared with their cycles of maximized energy output (CMEO). When σ is larger, the curve will shift to the right, allowing a similar maximized effective energy output E_{em} per cycle.[27] Connected with the proposed circuit, the output of the TENG can always be enhanced to approach the breakdown condition. The energy output of the threshold cycle is defined as the maximized energy output per cycle under the OM, E_{om}, which is summarized in Figure 1f and plotted in orange dots versus σ, as compared with ΔQ of the threshold cycle in blue dots. It simply shows the trends that with σ increases, the E_{om} decays while ΔQ increases.

By estimating eqs 1 and 2, it should be noticed that the energy stored in C_0 can be influenced by the capacitance of C_0 and the number n as well. Therefore, to reach a higher energy output and storage efficiency, the circuit is expanded to be the OM circuit, as shown in Figure 2a, in which the components in the dashed line frame is repeated by $n - 1$ times. The operation cycle under this OM is quite similar to that under the bennet's doubler, while the differences are briefly stated below: At point B, when V increases to nV_i, all C_0 are connected in series while being charged by the TENG. At point E, when V is decreased to be V_i, all C_0 are connected in parallel to charge the TENG. The output performance of the OM circuit is evaluated at C_0 = 300 nF, σ = 50 μC m^{-2}. Figure 2b shows simulated threshold cycles in the $V-Q$ plot along with the breakdown curve at different values of n, as calculated by the Paschen's law. Please notice that the breakdown may happen at V of only a few hundreds of volts, thus serving as a key limiting factor of the performance of TENGs.[7] The total charge transfer in the cycle decreases when n becomes larger, and the slope of point B to D as well as the voltage difference between A and B increases with n, resulting in a larger E_{om}. When n becomes larger, the TENG is easier to reach the breakdown condition and the slope of BD will become much larger, and finally the operation cycle is more like a triangle shape, resulting in decreased E_{om}. Equations for calculating ΔQ and V_i' are listed below, respectively

$$\Delta Q = \frac{\frac{\sigma S}{C_{1min}} + V_i\left(\frac{C_2}{C_{1min}} - n + 1\right)}{\frac{n}{C_0} + \frac{1}{C_{1min}} + \frac{1}{C_2}} \quad (3)$$

$$V_i' = \frac{\frac{(n-1)\sigma S}{C_{1min}} + nV_i(C_0 + C_2)\left(\frac{1}{C_0} + \frac{1}{C_{1min}} + \frac{1}{C_2}\right)}{\left(\frac{n}{C_0} + \frac{1}{C_{1min}} + \frac{1}{C_2}\right)(nC_0 + C_2)} \quad (4)$$

Derivations of these equations above are shown in Note S2.

Equations above show that the capacitance of C_0 is another important factor on the property of the OM. We choose n = 4 as an example for most simulations. Figure 2c,d shows the threshold cycles in the $V-Q$ plot with different capacitances of C_0 at σ of 50 μC m^{-2} and 70 μC m^{-2}, respectively, when n = 4. It can be seen from the operational cycle that when the capacitance C_0 is reduced, both BD and EA′ will shift upward, resulting in an increasing energy part by BD and a decreasing energy part by EA′; so the energy charge in the E_{om} is the sum of the two energy parts. Based on this, the relationship between E_{om} and the capacitance of C_0 is plotted in Figure 2e. Thus, C_0 = 10 nF can be considered as a good choice of capacitance as indicated by the dashed line, which can maintain a relatively high E_{om}, while its capacitance is large enough to avoid the parasitic-capacitance effect in circuits.[45−47]

In order to optimize the performance of the OM circuit, further studies are done by evaluating the output performance of the TENG at different capacitances and number n. The capacitance has very minimal impacts on ΔQ, as reflected by simulation results in Figure 3a, while the variation of E_{om}

https://dx.doi.org/10.1021/acsami.9b20060
ACS Appl. Mater. Interfaces 2020, 12, 5892−5900

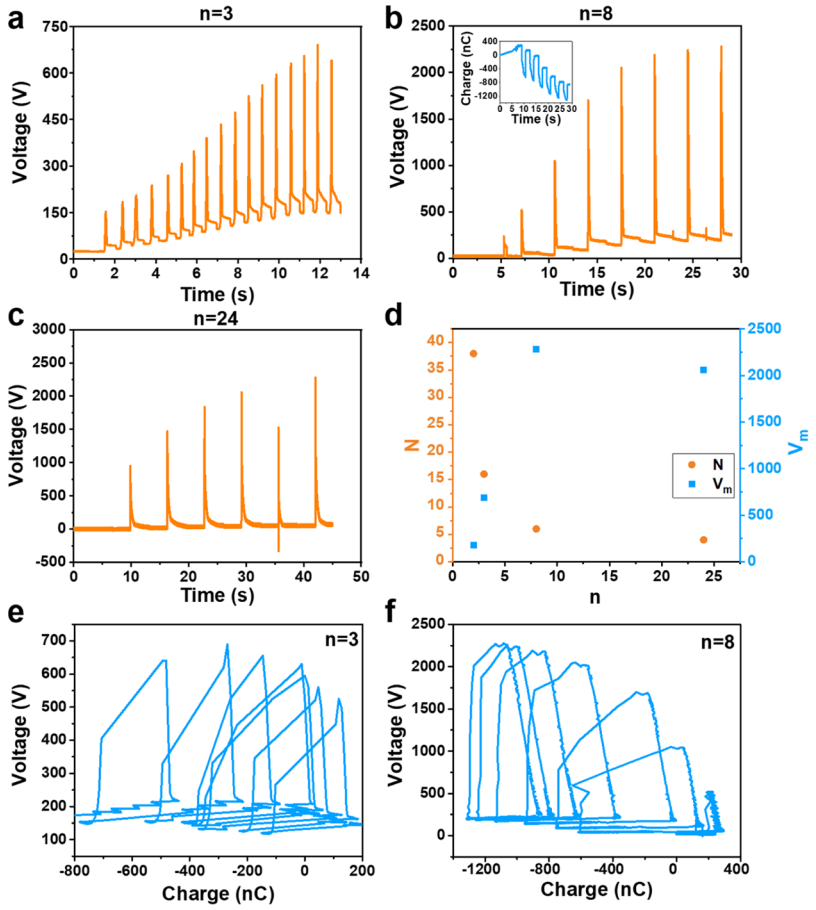

Figure 4. Experimental results of CS mode TENG under the OM. (a–c) Output voltage of TENG vs time at n = 3, 8, 24, respectively. Inset in (b) shows the charge output of TENG. Diverse peak in (c) shows the existence of breakdown. (d) Summary of N and the maximized output voltage of TENG at different n. (e,f) Experimental operation cycles of TENG in the V–Q plot at n = 3, 8, respectively. TENG is operated at σ = 50 μC m^{-2}.

depending on n and C_0 is plotted in Figure 3b. This indicates the trends that as n increases, E_{om} dramatically increases at a small n, while ΔQ always decreases with n, showing the ability of the OM circuit in enhancing the energy output of the TENG. However, due to the breakdown effect in the CS mode TENG, E_{om} is suppressed at n > 190, as illustrated in Figure 3c. The number of cycles N before reaching the breakdown condition from the initial voltage is plotted as Figure 3d, which will be influenced by C_0 and n as well. This implies that N is smaller when C_0 is smaller or n is larger, and when n > 8, N becomes a small number that can be easily achieved. When n = 30, breakdown will happen at the fourth cycle, indicating that the OM circuit becomes not practical with too many capacitors due to the breakdown effect. The E_{om} and the energy extraction ratio η of the TENG under the OM at different σ are summarized in Figure 3e, while the η is calculated by

$$\eta = \frac{E_{om}}{E_{em}} \times 100\% \tag{5}$$

where E_{em} is the theoretical maximum effective energy output with the breakdown effect considered, within CMEO.[41] This shows the ability of the OM circuit to extract energy from the TENG, compared with E_{em}, which can evaluate the merit of the OM circuit on power promotion. It can be noticed that a larger E_{om} under the OM can be realized at a smaller σ, which is always larger than 2.5 mJ when σ < 70 μC m^{-2}. The dramatic decay of E_{om} at $\sigma \geq$ 100 μC m^{-2} is because that it is so prone for the TENG to reach breakdown condition in just a few cycles that the promotion of its output performance is really limited. In experiments, identical surface charge density of the TENG can be maintained by compensational rubbing between the dielectric layer and nitrile glove. The figure also implies that η will improve as σ decays, and a η of 196% is realized at σ = 20 μC m^{-2} with n of 100, indicating the ability of the OM to promote the energy output of the TENG beyond E_{em}. It should be noticed that it is normal to have the η larger than 100% due to the greatly enhanced ΔQ, especially the negative charge part of the V–Q plot, which represents the generated energy outside the E_{om} cycle. At the same time, the super high η is achieved at a low σ, indicating the ability of the OM circuit to ensure the high output performance of TENGs with even low-performance triboelectric materials, which will greatly expand the application areas of TENGs. For example, in the high-temperature (400–600 K) environment, the triboelectric effect is usually limited by the thermionic emission and limited material selections.[48] While with the OM circuit, the output performance of TENGs with originally low triboelectric charge may be quickly promoted to be a high level in just a few cycles. This feature may enable the applications of TENGs in a harsh environment, including auto exhaust systems, thermal systems, and even outer space.

The charge enhancement ratio β is the other key parameter to evaluate the performance of the OM because the charge transferred by the circuit can be effectively utilized or stored,

https://dx.doi.org/10.1021/acsami.9b20060
ACS Appl. Mater. Interfaces 2020, 12, 5892–5900

compared with the high voltage source, except for E_{om}. It is defined as the ratio of the maximum charge output of the OM in the short-circuit condition over the total Q_{SC} of the TENG before reaching the breakdown condition

$$\beta = \frac{Q_{SC\_OM}}{NQ_{SC}} = \frac{V_m \times C_0}{NQ_{SC}} \quad (6)$$

Figure 3f shows that when with only 8 C_0, an 8-time charge enhancement can be achieved, and a larger n will lead to a larger β because V_m will increase while N will decrease. This multiplied charge output demonstrates the potential of using the OM for the PM function.

EXPERIMENTAL RESULTS AND DISCUSSION

To demonstrate the performance of the OM, circuits with different n and C_0 = 10 nF have been built. Figure 4 shows the experimental results of the CS mode TENG while connected with built circuits with different capacitor number n. Experimental parameters are listed in Table 2. The voltage outputs of the CS mode TENG with n = 3, 8, 24 are plotted in Figure 4a–c, respectively, with the surface charge density controlled at 50 μC m^{-2}, and the maximized voltage V_m is equivalent to that of point D in the threshold cycle. To correctly measure the high-voltage output, we designed the measurement method, as illustrated in Figure S2. The experimental results of V_m and N with different n are summarized in Figure 4d. The results imply that with the same initial surface charge density, the threshold voltage of the TENG is enhanced significantly at the beginning and then remains nearly the same as n increases, and the cycle number N required to approach the threshold cycle is decreased with n increasing as well, which are all consistent with the trends predicted by theoretical calculations. The charge output of the TENG while connected with the OM is shown in the inset in Figure 4b. The reverse peak in Figure 4c shows the existence of the breakdown effect, but the OM circuit still has the ability to continuously deliver the charge output. Further demonstration has been done by estimating the V–Q plots. Results are shown in Figure 4e for n = 3 and Figure 4f for n = 8, indicating the same trends in V_m and N. By integration in the V–Q plots, the E_{om} of n = 3, 8, 24 was calculated as 0.111, 0.789, and 0.335 mJ, respectively. Compared with the E_{em} of 7.834 mJ, an η of 10.07% was realized at n = 8, consistent with the theoretical η at n = 8, 9.97%. The difference between the experimental and theoretical results might be due to the measurement issues and the difficulty in controlling σ precisely. Other experimental results of different n are shown in Figure S3. These results also suggest that it is not applicable to continuously increase n because it is much more prone for the TENG to approach a breakdown condition at a larger n, leading to a dramatical decay in E_{om}. Based on eq 6, β of n = 3 is only 0.8625, while it is enhanced to 7.6 when n = 8 and 10.3 when n = 24. Therefore, parameters of the circuit are fixed as n = 8, C_0 = 10 nF for demonstrating the output performance as stated below.

Table 2. Experimental Parameters

initial surface charge density, σ	50 μC m^{-2}
structure parameters of CS mode TENG	l = w = 0.1 m
electrode material	copper
dielectric	FEM, 50 μm

Based on the working principle of the circuit, it is easy to understand that the energy stored in C_0 reaches the maximum at the point D of the threshold cycle. Therefore, to ensure the high energy storage efficiency, a switch S1 can be used to enable the energy storage only when the maximized voltage of C_0 is achieved. Figure 5a shows the OM circuit with a motion-triggered switch, in which an external capacitor C_e is applied to store the energy from the circuit, and the voltage of C_e shows the charge stored in the external capacitor. Here, n = 8 and σ = 50 μC m^2. During charging, the external capacitor C_e, several C_0 in the OM circuit are automatically connected in parallel, so that this OM circuit can also provide the PM function. By dynamic monitoring the voltage of C_0 through the circuit shown in Figure 5b, the switch will be turned on by hands when the voltage of C_0 reaches its maximum to charge the C_e. When the voltage of C_e in each charging process is saturated as observed, the switch is turned off, and then the next cycle begins. Dynamic measured results of voltages of C_0 and C_e are plotted in Figure 5c,d. When C_e = 1 μF, as shown in Figure 5c, where the voltage of C_0 is in orange and that of C_e is in blue, it can be noticed that with only several working cycles of the TENG, the voltage of C_e is charged up with a 10 V step each time, with the enlarged plot of the step shown in Figure 5f. Figure 5c is results of C_e = 100 nF with similar trends, while the charge transfer from C_0 to C_e is less than the former one, because more charges remain in C_0 due to the relative small capacitance of C_e. The charge transfer from C_0 to C_e is driven by the potential difference between OM and C_e, and when voltages of the OM and C_e are equivalent to each other, the charging process will stop. When C_e is relatively small, it can be easily charged to a high voltage level, as shown in Figure 5c,e, and more charges remain in the OM; so a larger C_e is preferred

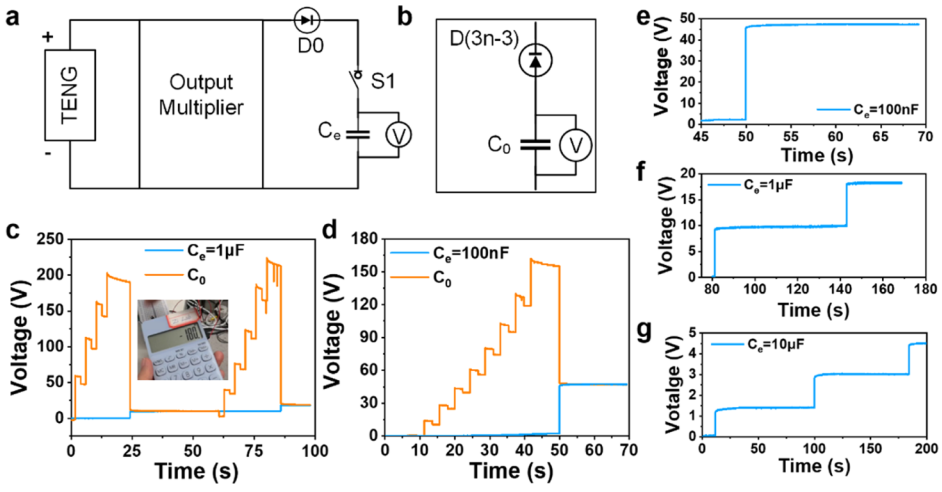

Figure 5. Experimental results of energy storage from the OM. (a) Circuit for energy storage from the OM and dynamic monitoring. S1 is a motion-triggered switch, and C_e is the capacitor for energy storage. (b) Circuit component for voltage monitoring of C_0. (c,d) Measured voltage of C_0 and C_e while TENG operated at σ = 50 μC m^{-2}, with C_e = 1 μF, 100 nF, respectively. (e–g) Enlarged plots of the measured voltage of C_e, with C_e = 100 nF, 1 μF, 10 μF, respectively.

https://dx.doi.org/10.1021/acsami.9b20060
ACS Appl. Mater. Interfaces 2020, 12, 5892–5900

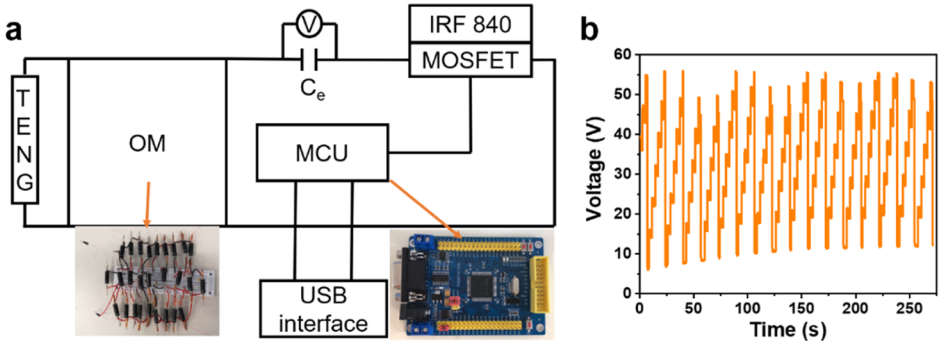

Figure 6. Experimental results of the OM with a smart switch. (a) Circuit of the OM with the smart switch circuit, which consists of a MOSFET and a MCU. Insets are photographs of the OM and the MCU. (b) Experimental results of the dynamic measurement for voltage of C_0. Improvement in the minimized voltage during operation shows the charged-up voltage of C_e.

to ensure a high energy storage efficiency. Figure 5g shows that when C_e = 10 μF, a 1.5 V step in voltage improvement is realized. With this OM circuit, the average charge output per cycle is ~2−2.5 μC at C_e = 1 μF and ~3−3.75 μC at C_e = 10 μF, which are significantly higher than that of the original TENG of 500 nC per cycle.

Furthermore, a smart switch was designed and constructed as S1 to realize the automatic control of the circuit, which would charge the energy storage capacitor C_e when the voltage of C_0 reaches the threshold voltage. The smart switch circuit is achieved by a MOSFET and a micro control unit (MCU), as shown in Figure 6a, with insets showing photographs of the OM and the MCU. A capacitor of 10 μF was selected for energy storage from the OM, which connects the OM circuit and MOSFET. Selection and construction of the MOSFET are described in Methods in detail. Similar to the motion triggered switch, the MOSFET is set to switch on at the threshold voltage of point D (V_D) to charge C_e in every T_s and switch off after a short period T_h. T_s means the time required before the OM reaches V_D, which is determined by the movement of the TENG and the voltage output of the OM. The working principle of the smart switch is described in Note S3. Figure 6b shows the measured voltage of C_0 while applying the smart switch circuit. The increase of the lowest point of each cycle confirms the automatic energy storage in C_e, demonstrating the functionality of the smart switch circuit. Dynamic monitoring of the measurement is shown in Video S1, implying that the whole system can work well to achieve automatic power promotion and management at the same time. As compared to the previous inductor-free PM system, threshold working frequency, bandwidth, and power input is not important for the OM because it can always enhance the charge output so the OM can be applied for various types of energy.

CONCLUSIONS

In conclusion, an inductor-free OM circuit that can promote and manage the output of the TENG simultaneously was proposed. Operation cycles in the $V-Q$ plot of this circuit were theoretically studied and experimentally demonstrated. Based on the maximum cycle, the maximized charge transfer ΔQ, the maximized energy output E_{om} of the TENG under the OM, and the number N of charging cycles for the TENG to approach the breakdown condition were analyzed in detail. It is found that a smaller capacitance of C_0 and a larger capacitor number n will contribute to a larger E_{om} and a smaller N, but the transferred charge will decay significantly with the increase of n, as demonstrated theoretically and experimentally. The E_{om} and η at different σ were also summarized, both showing increasing trends as σ decay. An η of 196% can be realized at σ = 20 μC m^2, reflecting the ability of OM to enhance the power output of the TENG with the low surface charge density. The OM with C_0 = 10 nF was built and operated at σ = 50 μC m^{-2}, and the E_{om} of 0.789 mJ and the β of 7.6 was realized at n = 8. By applying an external capacitor and a motion-triggered switch connected with the OM to store the energy, the average charge output per cycle was achieved ~2−2.5 μC at C_e = 1 μF and ~3−3.75 μC at C_e = 10 μF, implying significant improvement as compared with the original TENG of 500 nC per cycle. Furthermore, a smart controlled switch based on a MOSFET and a MCU is put forward to demonstrate the output performance. In summary, C_0 = 10 nF is a good capacitance for all conditions, while the selection of n depends on the applications. A higher charge enhancement ratio β can be achieved by a larger n, but the increase of n will always be limited by the breakdown effect in the TENG. Because of the breakdown limit, with a higher σ, usually a smaller n can be selected. When σ > 40 μC m^{-2}, n should not be larger than 10. This research provides a new method for the PM by an inductor-free design that is suitable for all TENGs; at the same time, it can promote the output performance of capacitance-variable TENGs significantly within several working cycles even at a very low surface charge density, which is essential for the development of TENG-based self-powered systems and industrial applications. This OM design may also provide a solution to promote TENG performance at various circumstances including the harsh environment.

METHODS

Electronics Selection. Diodes used in the OM are standard recovery diode, NTE517, purchased from element14.HK. NTE 517 is a silicon high voltage plastic power rectifier diode, with an electric breakdown voltage of 15 kV; so it is applicable for the high output voltage of the TENG. MOSFET IRF 840 was selected to realize the controllable switch function. IRF 840 has good performance in switch characteristic, which could bear max D−S voltage at 500 V, and the D−S resistant is smaller than 0.85 Ω. The drain terminal of MOSFET is connected with an energy storage capacitor, the source terminal is connected with a negative electrode of management circuit, and the gate terminal is connected with an MCU interface.

Fabrication of the TENG. The TENG used in this research is a CS mode TENG with a triboelectric area of 10 cm × 10 cm. The material of the electrode is copper, and dielectric is FEP. One electrode layer is fabricated by a copper tape pasted on an acrylic substrate, and the other electrode is fabricated by e-beam evaporation on the FEP film and then pasted on an acrylic substrate by Kapton tape.

Measurement. The voltage of the TENG is measured by a SRS570 filter to measure the current and a resistor of 5 GΩ connected in series. Transferred charge and dynamic monitoring for voltage of C_0 are measured by Keithley6514.

https://dx.doi.org/10.1021/acsami.9b20060
ACS Appl. Mater. Interfaces 2020, 12, 5892−5900

■ ASSOCIATED CONTENT

Supporting Information

The Supporting Information is available free of charge at https://pubs.acs.org/doi/10.1021/acsami.9b20060.

Detailed description of the operation principle of the doubler and the multiplier; detailed description of the working principle of the smart switch circuit (PDF)

Dynamic monitoring for C_e applied to power the calculator (MP4)

Dynamic output measurement for the OM with the smart switch circuit (MP4)

■ AUTHOR INFORMATION

Corresponding Author

Yunlong Zi − *The Chinese University of Hong Kong, Shatin, China;* orcid.org/0000-0002-5133-4057; Email: ylzi@cuhk.edu.hk

Other Authors

Xin Xia − *The Chinese University of Hong Kong, Shatin, China*

Haoyu Wang − *The Chinese University of Hong Kong, Shatin, China*

Philippe Basset − *Université Paris-Est, ESYCOM, ESIEE Paris-CNAM-UPEM, Noisy-le-Grand, France;* orcid.org/0000-0002-9790-8247

Yuyan Zhu − *The Hong Kong Polytechnic University, Kowloon, China*

Complete contact information is available at: https://pubs.acs.org/10.1021/acsami.9b20060

Author Contributions

X.X., H.W., and Y.Z. conceived the idea, discussed the results and prepared the manuscript. X.X. and Y.Z. analyzed the working principle and designed the OM circuit. X.X. did the theoretical simulation of the OM circuit. X.X. fabricated the CS mode TENGs and constructed the OM circuit. H.W. designed and constructed the smart switch circuit. X.X. and H.W. did the electrical measurement. X.X. analyzed the experiment data. P.B. and Y.Z. helped on discussions and preparation of the manuscript.

Notes

The authors declare no competing financial interest.

The data that support the findings of this study are available from the corresponding author upon reasonable request.

■ ACKNOWLEDGMENTS

This work was funded by HKSAR Innovation and Technology Support Program Tier 3 (grant no. ITS/085/18), Shun Hing Institute of Advanced Engineering (grant no. RNE-p5-18), and The Chinese University of Hong Kong Direct Grant (grant no. 4055086).

■ REFERENCES

(1) Fan, F.-R.; Tian, Z.-Q.; Lin Wang, Z. Flexible Triboelectric Generator. *Nano Energy* **2012**, *1*, 328−334.

(2) Wang, Z. L. Triboelectric Nanogenerators as New Energy Technology for Self-Powered Systems and as Active Mechanical and Chemical Sensors. *ACS Nano* **2013**, *7*, 9533−9557.

(3) Zhu, G.; Pan, C.; Guo, W.; Chen, C.-Y.; Zhou, Y.; Yu, R.; Wang, Z. L. Triboelectric-Generator-Driven Pulse Electrodeposition for Micropatterning. *Nano Lett.* **2012**, *12*, 4960−4965.

(4) Niu, S.; Liu, Y.; Wang, S.; Lin, L.; Zhou, Y. S.; Hu, Y.; Wang, Z. L. Theory of Sliding-Mode Triboelectric Nanogenerators. *Adv. Mater.* **2013**, *25*, 6184−6193.

(5) Niu, S.; Liu, Y.; Chen, X.; Wang, S.; Zhou, Y. S.; Lin, L.; Xie, Y.; Wang, Z. L. Theory of Freestanding Triboelectric-Layer-Based Nanogenerators. *Nano Energy* **2015**, *12*, 760−774.

(6) Niu, S.; Wang, Z. L. Theoretical Systems of Triboelectric Nanogenerators. *Nano Energy* **2015**, *14*, 161−192.

(7) Niu, S.; Wang, S.; Lin, L.; Liu, Y.; Zhou, Y. S.; Hu, Y.; Wang, Z. L. Theoretical Study of Contact-Mode Triboelectric Nanogenerators as An Effective Power Source. *Energy Environ. Sci.* **2013**, *6*, 3576.

(8) Zhang, S. L.; Xu, M.; Zhang, C.; Wang, Y.-C.; Zou, H.; He, X.; Wang, Z.; Wang, Z. L. Rationally Designed Sea Snake Structure Based Triboelectric Nanogenerators for Effectively and Efficiently Harvesting Ocean Wave Energy with Minimized Water Screening Effect. *Nano Energy* **2018**, *48*, 421−429.

(9) Wang, Z. L.; Jiang, T.; Xu, L. Toward the Blue Energy Dream by Triboelectric Nanogenerator Networks. *Nano Energy* **2017**, *39*, 9−23.

(10) Luo, J.; Xu, L.; Tang, W.; Jiang, T.; Fan, F. R.; Pang, Y.; Chen, L.; Zhang, Y.; Wang, Z. L. Direct-Current Triboelectric Nanogenerator Realized by Air Breakdown Induced Ionized Air Channel. *Adv. Energy Mater.* **2018**, *8*, 1800889.

(11) Su, Y.; Wen, X.; Zhu, G.; Yang, J.; Chen, J.; Bai, P.; Wu, Z.; Jiang, Y.; Lin Wang, Z. Hybrid Triboelectric Nanogenerator for Harvesting Water Wave Energy and as A Self-Powered Distress Signal Emitter. *Nano Energy* **2014**, *9*, 186−195.

(12) Chen, B.; Yang, Y.; Wang, Z. L. Scavenging Wind Energy by Triboelectric Nanogenerators. *Adv. Energy Mater.* **2018**, *8*, 1702649.

(13) Olsen, M.; Zhang, R.; Ortegren, J.; Andersson, H.; Yang, Y.; Olin, H. Frequency and Voltage Response of A Wind-Driven Fluttering Triboelectric Nanogenerator. *Sci. Rep.* **2019**, *9*, 5543.

(14) Seol, M.-L.; Woo, J.-H.; Jeon, S.-B.; Kim, D.; Park, S.-J.; Hur, J.; Choi, Y.-K. Vertically Stacked Thin Triboelectric Nanogenerator for Wind Energy Harvesting. *Nano Energy* **2015**, *14*, 201−208.

(15) Yang, Y.; Zhu, G.; Zhang, H.; Chen, J.; Zhong, X.; Lin, Z.-H.; Su, Y.; Bai, P.; Wen, X.; Wang, Z. L. Triboelectric Nanogenerator for Harvesting Wind Energy and as Self-Powered Wind Vector Sensor System. *ACS Nano* **2013**, *7*, 9461−9468.

(16) Wang, J.; Li, S.; Yi, F.; Zi, Y.; Lin, J.; Wang, X.; Xu, Y.; Wang, Z. L. Sustainably Powering Wearable Electronics Solely by Biomechanical Energy. *Nat. Commun.* **2016**, *7*, 12744.

(17) Wen, Z.; Yang, Y.; Sun, N.; Li, G.; Liu, Y.; Chen, C.; Shi, J.; Xie, L.; Jiang, H.; Bao, D.; Zhuo, Q.; Sun, X. A. Wrinkled PEDOT:PSS Film Based Stretchable and Transparent Triboelectric Nanogenerator for Wearable Energy Harvesters and Active Motion Sensors. *Adv. Funct. Mater.* **2018**, *28*, 1803684.

(18) Xiong, J.; Cui, P.; Chen, X.; Wang, J.; Parida, K.; Lin, M. F.; Lee, P. S. Skin-Touch-Actuated Textile-Based Triboelectric Nanogenerator with Black Phosphorus for Durable Biomechanical Energy Harvesting. *Nat. Commun.* **2018**, *9*, 4280.

(19) Dhakar, L.; Pitchappa, P.; Tay, F. E. H.; Lee, C. An Intelligent Skin Based Self-Powered Finger Motion Sensor Integrated with Triboelectric Nanogenerator. *Nano Energy* **2016**, *19*, 532−540.

(20) Bai, P.; Zhu, G.; Lin, Z.-H.; Jing, Q.; Chen, J.; Zhang, G.; Ma, J.; Wang, Z. L. Integrated Multilayered Triboelectric Nanogenerator for Harvesting Biomechanical Energy From Human Motions. *ACS Nano* **2013**, *7*, 3713−3719.

(21) Zhang, H.; Yang, Y.; Su, Y.; Chen, J.; Adams, K.; Lee, S.; Hu, C.; Wang, Z. L. Triboelectric Nanogenerator for Harvesting Vibration Energy in Full Space and as Self-Powered Acceleration Sensor. *Adv. Funct. Mater.* **2014**, *24*, 1401−1407.

(22) Yang, W.; Chen, J.; Zhu, G.; Wen, X.; Bai, P.; Su, Y.; Lin, Y.; Wang, Z. Harvesting Vibration Energy by a Triple-Cantilever Based Triboelectric Nanogenerator. *J. Nano Res.* **2013**, *6*, 880−886.

(23) Chen, J.; Zhu, G.; Yang, W.; Jing, Q.; Bai, P.; Yang, Y.; Hou, T.-C.; Wang, Z. L. Harmonic-Resonator-Based Triboelectric Nano-

generator as a Sustainable Power Source and a Self-Powered Active Vibration Sensor. *Adv. Mater.* **2013**, *25*, 6094−6099.
(24) Wang, Z. L. On Maxwell's Displacement Current for Energy and Sensors: the Origin of Nanogenerators. *Mater. Today* **2017**, *20*, 74−82.
(25) Xu, C.; Zi, Y.; Wang, A. C.; Zou, H.; Dai, Y.; He, X.; Wang, P.; Wang, Y. C.; Feng, P.; Li, D.; Wang, Z. L. On the Electron-Transfer Mechanism in the Contact-Electrification Effect. *Adv. Mater.* **2018**, *30*, 1706790.
(26) Lin, S.; Xu, L.; Xu, C.; Chen, X.; Wang, A. C.; Zhang, B.; Lin, P.; Yang, Y.; Zhao, H.; Wang, Z. L. Electron Transfer in Nanoscale Contact Electrification: Effect of Temperature in the Metal-Dielectric Case. *Adv. Mater.* **2019**, *31*, 1808197.
(27) Zi, Y.; Wu, C.; Ding, W.; Wang, Z. L. Maximized Effective Energy Output of Contact-Separation-Triggered Triboelectric Nanogenerators as Limited by Air Breakdown. *Adv. Funct. Mater.* **2017**, *27*, 1700049.
(28) Dorzhiev, V.; Karami, A.; Basset, P.; Marty, F.; Dragunov, V.; Galayko, D. Electret-Free Micromachined Silicon Electrostatic Vibration Energy Harvester With the Bennet's Doubler as Conditioning Circuit. *IEEE Electron Device Lett.* **2015**, *36*, 183−185.
(29) de Queiroz, A. C. M.; Domingues, M. The Doubler of Electricity Used as Battery Charger. *IEEE Trans. Circuits Syst.* **2011**, *58*, 797−801.
(30) Truong, B. D.; Phu Le, C.; Halvorsen, E. Analysis of Electrostatic Energy Harvesters Electrically Configured as Bennet's Doublers. *IEEE Sens. J.* **2017**, *17*, 5180−5191.
(31) Ghaffarinejad, A.; Hasani, J. Y.; Hinchet, R.; Lu, Y.; Zhang, H.; Karami, A.; Galayko, D.; Kim, S.-W.; Basset, P. A Conditioning Circuit with Exponential Enhancement of Output Energy for Triboelectric Nanogenerator. *Nano Energy* **2018**, *51*, 173−184.
(32) Karami, A.; Galayko, D.; Basset, P. Series-Parallel Charge Pump Conditioning Circuits for Electrostatic Kinetic Energy Harvesting. *IEEE Trans. Circuits Syst.* **2017**, *64*, 227−240.
(33) Cui, N.; Gu, L.; Lei, Y.; Liu, J.; Qin, Y.; Ma, X.; Hao, Y.; Wang, Z. L. Dynamic Behavior of the Triboelectric Charges and Structural Optimization of the Friction Layer for a Triboelectric Nanogenerator. *ACS Nano* **2016**, *10*, 6131−6138.
(34) Wang, J.; Wu, C.; Dai, Y.; Zhao, Z.; Wang, A.; Zhang, T.; Wang, Z. L. Achieving Ultrahigh Triboelectric Charge Density for Efficient Energy Harvesting. *Nat. Commun.* **2017**, *8*, 88.
(35) Lee, K. Y.; Chun, J.; Lee, J.-H.; Kim, K. N.; Kang, N.-R.; Kim, J.-Y.; Kim, M. H.; Shin, K.-S.; Gupta, M. K.; Baik, J. M.; Kim, S.-W. Hydrophobic Sponge Structure-Based Triboelectric Nanogenerator. *Adv. Mater.* **2014**, *26*, 5037−5042.
(36) Jeong, C. K.; Baek, K. M.; Niu, S.; Nam, T. W.; Hur, Y. H.; Park, D. Y.; Hwang, G.-T.; Byun, M.; Wang, Z. L.; Jung, Y. S.; Lee, K. J. Topographically-Designed Triboelectric Nanogenerator via Block Copolymer Self-Assembly. *Nano Lett.* **2014**, *14*, 7031−7038.
(37) Xi, F.; Pang, Y.; Li, W.; Jiang, T.; Zhang, L.; Guo, T.; Liu, G.; Zhang, C.; Wang, Z. L. Universal Power Management Strategy for Triboelectric Nanogenerator. *Nano Energy* **2017**, *37*, 168−176.
(38) Zhu, G.; Chen, J.; Zhang, T.; Jing, Q.; Wang, Z. L. Radial-Arrayed Rotary Electrification for High Performance Triboelectric Generator. *Nat. Commun.* **2014**, *5*, 3426.
(39) Cheng, X.; Miao, L.; Song, Y.; Su, Z.; Chen, H.; Chen, X.; Zhang, J.; Zhang, H. High Efficiency Power Management and Charge Boosting Strategy for A Triboelectric Nanogenerator. *Nano Energy* **2017**, *38*, 438−446.
(40) Qin, H.; Cheng, G.; Zi, Y.; Gu, G.; Zhang, B.; Shang, W.; Yang, F.; Yang, J.; Du, Z.; Wang, Z. L. High Energy Storage Efficiency Triboelectric Nanogenerators with Unidirectional Switches and Passive Power Management Circuits. *Adv. Funct. Mater.* **2018**, *28*, 1805216.
(41) Zi, Y.; Wang, J.; Wang, S.; Li, S.; Wen, Z.; Guo, H.; Wang, Z. L. Effective Energy Storage from A Triboelectric Nanogenerator. *Nat. Commun.* **2016**, *7*, 10987.
(42) Zi, Y.; Guo, H.; Wang, J.; Wen, Z.; Li, S.; Hu, C.; Wang, Z. L. An Inductor-Free Auto-Power-Management Design Built-in Triboelectric Nanogenerators. *Nano Energy* **2017**, *31*, 302−310.
(43) Wang, S.; Xie, Y.; Niu, S.; Lin, L.; Liu, C.; Zhou, Y. S.; Wang, Z. L. Maximum Surface Charge Density for Triboelectric Nanogenerators Achieved by Ionized-Air Injection: Methodology and Theoretical Understanding. *Adv. Mater.* **2014**, *26*, 6720−6728.
(44) Li, Y.; Li, Q. Computation of Electrostatic Forces with Edge Effects for Non-Parallel Comb-Actuators. *J. Tsinghua Univ.* **2003**, *43*, 1024−1026+1030.
(45) Dai, K.; Wang, X.; Niu, S.; Yi, F.; Yin, Y.; Chen, L.; Zhang, Y.; You, Z. Simulation and Structure Optimization of Triboelectric Nanogenerators Considering the Effects of Parasitic Capacitance. *J. Nano Res.* **2016**, *10*, 157−171.
(46) Jiang, T.; Chen, X.; Han, C. B.; Tang, W.; Wang, Z. L. Theoretical Study of Rotary Freestanding Triboelectric Nanogenerators. *Adv. Funct. Mater.* **2015**, *25*, 2928−2938.
(47) Peng, J.; Kang, S. D.; Snyder, G. J. Optimization Principles and the Figure of Merit for Triboelectric Generators. *Sci. Adv.* **2017**, *3*, No. eaap8576.
(48) Xu, C.; Wang, A. C.; Zou, H.; Zhang, B.; Zhang, C.; Zi, Y.; Pan, L.; Wang, P.; Feng, P.; Lin, Z.; Wang, Z. L. Raising the Working Temperature of a Triboelectric Nanogenerator by Quenching Down Electron Thermionic Emission in Contact-Electrification. *Adv. Mater.* **2018**, *30*, 1803968.

https://dx.doi.org/10.1021/acsami.9b20060
ACS Appl. Mater. Interfaces 2020, 12, 5892−5900